On the control design and robustness analysis for high-density microcantilever arrays

Azeem Sarwar, Petros G Voulgaris and Srinivasa M Salapaka

Journal of Vibration and Control 2011 17: 1195 originally published online 8 November 2010

DOI: 10.1177/1077546310381038

Article

Journal of Vibration and Control
17(8) 1195–1210

DOI: 10.1177/1077546310381038
jvc.sagepub.com
SAGE

On the control design and robustness analysis for high-density microcantilever arrays

Azeem Sarwar[1], Petros G Voulgaris[2] and Srinivasa M Salapaka[1]

Abstract

In this paper we present a basic model and control design of an array of electrostatically actuated microcantilevers. Part of the main focus of this paper is to study the feasibility and compare the performance of the centralized, decentralized and distributed schemes on a microcantilever array system. Since the implementation of a centralized controller for such systems is impractical, we consider the following two control schemes with localized architecture: (a) a $\mathcal{H}_\infty$ decentralized controller that completely ignores the dynamics contributed by the neighbors hence treating them as an external disturbance; and (b) a $\mathcal{H}_\infty$ distributed controller that makes use of information only from its immediate neighbors. In order to have some benchmark performance index, we first design a $\mathcal{H}_\infty$ centralized controller for an array of eight microcantilevers. The performance of these controllers are tested via simulations on a finite nonlinear model of the system, and compared with the benchmark performance delivered by the centralized controller. It is seen that the performance delivered by a distributed controller is quite comparable to the performance delivered by the benchmark scheme of a centralized controller. In comparison, the performance of the decentralized controller degrades by more than 100% in terms of resolution. Another main contribution of this paper is the robustness analysis with respect to the modeling uncertainties. This is important, especially in the view of the fabrication errors which result in deviation of actual dynamics of each microcantilever from its model, as well as since the control designs are derived from a linearized model of the cantilever array. In this direction, analysis and simulations of control implementations on perturbed linear as well as nonlinear models of system with finite microcantilever arrays are presented.

Keywords

AFM, distributed control, array architecture, atomic force microscope, nano

Received: 8 December 2008; accepted: 4 February 2009

1. Introduction

The invention of atomic force microscopy (AFM), and closely related technologies which use microcantilever-based sensing, have revolutionized research in various areas such as biology, materials science, optics, precision mechanics, and micro-electronics (Bhushan, 1995; Crandall, 1996; Yves, 1995). The demonstration of their capability of interrogation, control and manipulation of matter at the atomic scale, together with the capability of sensing a variety of physical signals in diverse environments is having a dramatic impact in fields as diverse as biology, materials science, electrochemistry, tribology, biochemistry, surface physics, and medicine.

In many nanoscientific studies, large areas with characteristic lengths of at least on the order of millimeters or micrometers are needed to be investigated with nanoscale precision. This requires high-bandwidth scanning capability which most existing devices lack. In spite of significant advances in the last two decades, the status of research and development in the context of microcantilever-based devices

[1]Mechanical Science and Engineering, University of Illinois at Urbana-Champaign, Urbana-Champaign, IL, USA
[2]Department of Aerospace Engineering, University of Illinois at Urbana-Champaign, Urbana-Champaign, IL, USA

Corresponding author:
Azeem Sarwar, Mechanical Science and Engineering, University of Illinois at Urbana-Champaign, Urbana, IL, USA
Email: asarwar@illinois.edu

is still at its preliminary stages. Most of the current research and technology is based on single cantilever mechanisms, which provide sequential and therefore slow investigation. Consequently, there is a large impetus on increasing the bandwidth and throughput of these devices while guaranteeing reliable nanoscale precision. This calls for extending the single cantilever technology to multicantilever-based systems to make high-throughput nanoscale investigation viable. This need is further fuelled by certain high-throughput applications, which if successful, will have a significant impact on the current science and industry. For instance, by coating the cantilever tip with particular types of biomolecules or chemicals, the absorption of reactant molecules or chemicals onto the cantilever are detected through changes in its mass, hence its resonance frequency, or through changes in the surface stress. The possibilities that this method, when extended to multicantilever systems, offers to gene scanning and chemical sensing is enormous and is predicted to have a huge impact on the area of combinatorial drug discovery. Similarly, the development of multicantilever-based devices is expected to revolutionize combinatorial chemistry and material investigation. The capability to write and read information from the surface by depositing, removing or modifying material from the tip and/or sample, when extended from single cantilever-based nanolithography to multicantilever systems, will give six orders increase in the information densities of storage media (Pantazi et al., 2008).

At present, however, the research that scales up through multicantilever-based mechanisms is at the developmental stage. There are some prototypes of multicantilever devices (Britton et al., 2000; Despant et al., 2000; Indermühle et al., 1997; Pantazi et al., 2008) and it is not expected to be long before reliable products with individual actuation and sensing of cantilever units become commercially available. Our research focuses on the immediate next step, that is, to provide an efficient control scheme for effective use of such multicantilever-based devices to successfully allow independent actuation without compromising the packing density (number of cantilever units per unit area), and therefore the device throughput. In typical current designs, the coupling effects are ignored, and to avoid the coupling effects, the packing density is reduced thereby compromising on the throughput.

Recently, the work reported by Napoli et al. provides extensive analysis and control design for multicantilever systems (including distributed control design (Napoli and Bamieh, 2001; Napoli et al., 1998) for different objectives) as well as address a number of issues with them (Napoli, 2004; Napoli and Bamieh, 2001, 2004; Napoli et al., 1998, 2003, 2004, 2005a,b). They have modeled and presented a detailed dynamic analysis of closely packed microcantilever arrays where they have considered different sources of coupling, such as electrostatic and mechanical (Napoli and Bamieh, 2001; Napoli et al., 2005b), as well as different actuation schemes that include piezoelectric (Napoli et al., 1998) and capacitive (Napoli and Bamieh, 2001; Napoli et al., 2004, 2005a) schemes. Experimental studies on a two-cantilever system are presented in Napoli et al. (2005b). These studies of models of densely packed cantilever arrays emphasize that the parallelism together with tight packing of cantilever units introduces dynamic coupling between the individual units (Napoli, 2004).

This paper is along the lines of the above work. We analyze and present a control design for tightly packed microcantilever arrays. The model derived for electrostatically actuated microcantilever arrays is of a similar form to that considered in Napoli and Bamieh (2001) and Napoli et al. (2005b). Part of the main focus of this paper is to compare the feasibility and performance of the centralized, decentralized and distributed schemes on a microcantilever array system. After developing control designs based on robust control theory ($\mathcal{H}_\infty$ control designs) for centralized and decentralized schemes, and using the recent tools developed by Bamieh et al. (2002) for exploiting the spatial invariance structure for the distributed scheme, we provide an extensive numerical simulation study to compare them. The results show that distributed control designs where each cantilever communicates with a couple of its neighbors approximately retrieves the performance of the benchmark, albeit practically infeasible, centralized scheme, whereas the decentralized scheme severely underperforms when compared with the benchmark. Another main contribution of this paper is the robustness analysis with respect to the modeling uncertainties. This is important, especially in the view of the fabrication errors which result in deviation of actual dynamics of each microcantilever from its model, as well as since the control designs are derived from a linearized model of the cantilever array. In this direction, analysis and simulations of control implementations on perturbed linear as well as nonlinear models of systems with finite microcantilever arrays are presented. This analysis also aims at finding critical parameters in the physical system that the control designs are extremely sensitive to. For instance, the results show that the system behavior is significantly more sensitive to changes in the natural frequencies of the cantilever when compared with other lumped parameters in the design.

This paper is organized as follows. The modeling and description of the system are presented in the next section. This is followed by a presentation of $\mathcal{H}_\infty$ centralized controller design for a system of a finite microcantilever array in order to have some benchmark performance index. We next consider an

uncoupled system, thereby treating the coupled dynamics as external disturbances for which efficient $\mathcal{H}_\infty$ disturbance rejection routine is sought. This is followed by a discussion on the formulation of a $\mathcal{H}_\infty$ distributed controller architecture for the problem in question. Finally, we conclude with some observations in the last section.

2. System modeling and description

The geometry of the abstract system considered is shown in Figure 1(a). (The details of the mechanical characteristics of system can be found in the Appendix). It is based on extending the two-cantilever system considered in Napoli et al. (2005b) to larger arrays. The system consists of infinitely many micro-cantilevers connected to a base, each forming a micro-capacitor, with the second rigid plate located underneath the microcantilever. The microcantilever is flexible and can move in the vertical axis, however it is assumed to be rigid along the horizontal axis. The vertical displacement of each microcantilever can be controlled by applying a voltage across the plates. Although each microcantilever is actuated independently, its dynamics are influenced by the presence of other microcantilevers. As elaborated in Figure 1(a), this coupling has two sources of origin: (1) mechanical, since the microcantilevers are attached to the same base and (2) electrical, due to the fringing fields generated by the micro-capacitors nearby. The force acting on each microcantilever can be split in its components along the three axes. Since the microcantilevers are assumed to be nonrigid only along the vertical axis, the equation of motion only for the vertical displacement z_i is considered. For $i \in \mathbb{Z}$ (integers), we can write the equation of motion of each microcantilever as

$$\ddot{z}_i + b\dot{z}_i + \omega^2 z_i = F_{a,i} + F_{\text{mech},i} + F^{\perp}_{\text{elec},i} \tag{1}$$

where b is the normalized damping coefficient (Napoli et al., 2004) and ω is the natural resonant frequency of the ith microcantilever beam (Napoli et al., 2003). $F_{a,i}$ is the attractive force between the micro-capacitor plates of the ith microcantilever and is given by the following expression

$$F_{a,i} = \frac{\epsilon_0 A}{2md^2}\left(1 + \frac{2z_i}{d}\right)U_i^2 \tag{2}$$

where ϵ_0, d, A, m, U_i represent, respectively, the permittivity in vacuum, the gap between the electrodes, the area of the micro-capacitor plates, the mass of the microcantilever, and the voltage applied across the ith cantilever unit. $F_{\text{mech},i}$ is an equivalent mechanical coupling force exerted on the ith microcantilever by its neighbors and is given by the following expression

$$F_{\text{mech},i} = \frac{1}{m}\sum_{j=i-1,\ j\neq i}^{i+1} \gamma_{i,j}(z_j - z_i) \tag{3}$$

where $\gamma_{i,j}$ is the coefficient of mechanical coupling (Napoli and Bamieh, 2004). $F^{\perp}_{\text{elec},i}$ is the electrostatic coupling force exerted on the ith microcantilever beam by its neighbors and is given by the following expression

$$F^{\perp}_{\text{elec},i} = \frac{c_i U_i}{m4\pi\epsilon_0}\sum_{j=-\infty,\ j\neq i}^{\infty} \frac{c_j U_j (z_i - z_j)}{r_{i,j}^3} \tag{4}$$

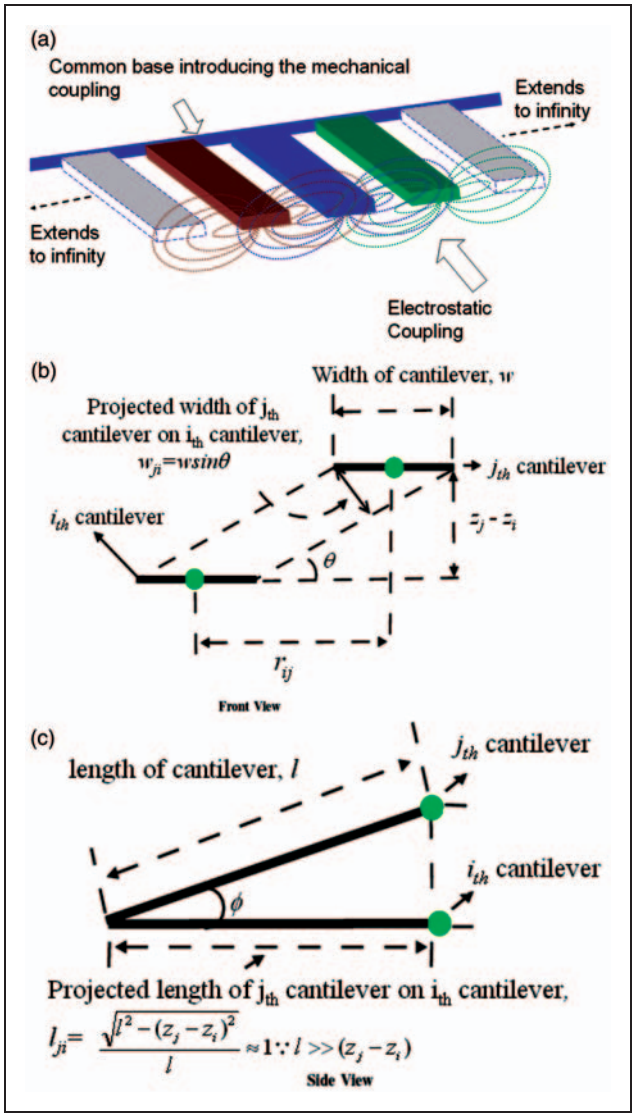

Figure 1. (a) Schematic showing the layout of the infinite-dimensional microcantilever array with mechanical and electrostatic coupling. Each capacitor unit in the array consists of two plates (200 μm × 5 μm) that are separated by 2 μm, each of which is fixed to a substrate at one end. One of the plates is flexible (cantilever) while the other is rigid. The cantilever oscillation amplitudes are of the order of 200 nm. (b), (c) Projected area of the jth microcantilever on the ith microcantilever.

where c_i and c_j are the capacitances of the ith and jth microcantilever, respectively, U_i and U_j are the voltages applied across the ith and jth microcantilever, respectively, and $r_{i,j}$ is the horizontal distance between the centroids of ith and jth microcantilever.

2.1. Mechanical coupling

Based on Napoli (2004), the mechanical coupling has been modeled as a spring-like force, proportional to the difference in the vertical displacement z_i of the microcantilevers. The effect of mechanical coupling is localized in the sense that only a finite (two) number of neighbors contribute towards the coupling as evident from Equation (3).

2.2. Electrostatic coupling

Following the arrangement in Napoli et al. (2003), the voltage applied to each micro-capacitor is considered to be inducing a charge on its neighbors. Specifically the following expression is considered for the charge on the ith plate:

$$q_i = c_i U_i + \sum_{j=-\infty, j\neq i}^{\infty} c_{i,j} U_{i,j} \quad \text{where } c_i = \epsilon_0 \frac{A}{d - z_i} \tag{5}$$

Using the parallel plate capacitor theory, $c_{i,j} = \epsilon_0 (A_{i,j}/d_{i,j})$ where $A_{i,j}$ is the projected area of jth microcantilever onto the ith microcantilever and $d_{i,j}$ is the displacement between the centroid of the ith and the jth microcantilever. Referring to Figure 1(b) and (c) the area projected by the jth microcantilever on the ith microcantilever is given by

$$A_{i,j} = w_{i,j} \times l_{i,j} = w \frac{(z_j - z_i)^2}{\sqrt{r_{i,j}^2 + (z_i - z_j)^2}} \tag{6}$$

The corresponding expression for the capacitance $c_{i,j}$, is therefore given as follows

$$c_{i,j} = \epsilon_0 \frac{w(z_j - z_i)^2}{r_{i,j}^2 + (z_i - z_j)^2} \tag{7}$$

The plot of the charge induced on the ith microcantilever due to the voltage U_i applied across itself, along with the charge induced on it by its neighbors because of the voltage $U_{i,j} = U_i - U_j$, is presented in Figure 2. The total resulting charge (up to 30 neighbors, 15 on each side) is also shown. It can be seen that the charge induced by the neighboring microcantilevers asymptotes quite rapidly as we move away from the reference microcantilever. This is also evident from the expression of $c_{i,j}$ where the presence of the term $r_{i,j}^2$ in the denominator ensures the rapid decay of $c_{i,j}$ as we move away from the reference microcantilever. It can also be seen from Figure 2 that the contribution of

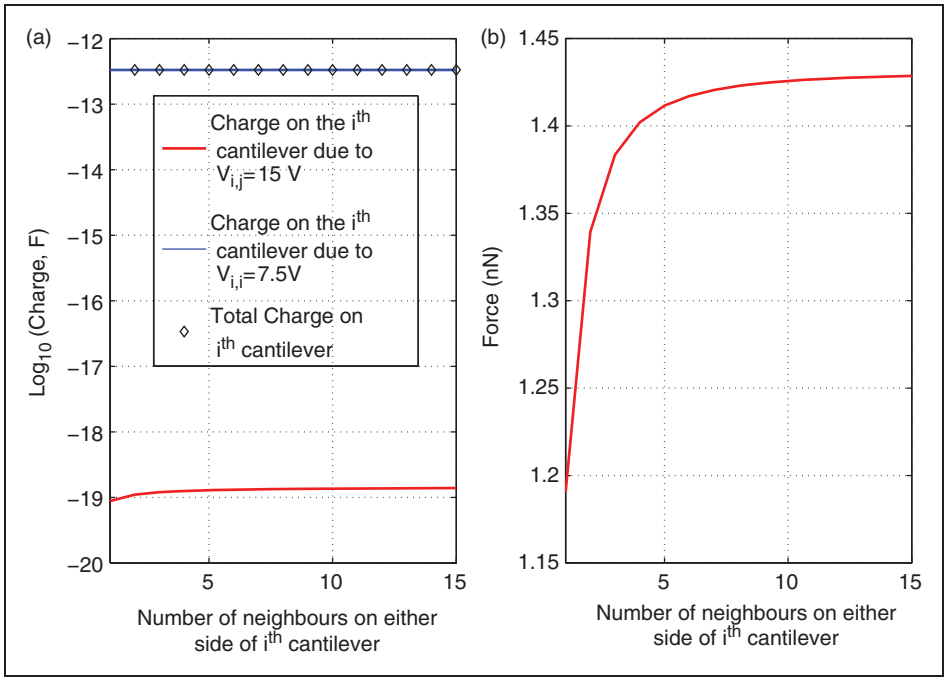

Figure 2. (a) Charge contributed by the neighbors on the ith microcantilever and (b) electrostatic coupling force exerted by the neighbors on the ith microcantilever.

charge induced by the neighbors on the reference microcantilever is insignificant, and hence the expression $\sum_{j=-\infty, j\neq i}^{\infty} c_{i,j}U_{i,j}$ was neglected in rest of the analysis.

The charges induced on each microcantilever result in an electrostatic interaction amongst the microcantilevers. As in Napoli et al. (2003), the interaction between these induced charges is described via a point charge model. Each microcantilever is represented as a charged particle, q_i, and the mutual interaction is described by the Coulomb's law

$$F_{\text{elec},i} = \frac{c_i U_i}{4\pi\epsilon_0} \sum_{j=-\infty, j\neq i}^{\infty} \frac{c_j U_j}{r_{i,j}^2} \tag{8}$$

and the vertical component of this force is given as

$$\begin{aligned} F_{\text{elec},i}^{\perp} &= \frac{c_i U_i}{4\pi\epsilon_0} \sum_{j=-\infty, j\neq i}^{\infty} \frac{c_j U_j (z_i - z_j)}{r_{i,j}^2 \sqrt{r_{i,j}^2 + (z_i - z_j)^2}} \\ &\approx \frac{c_i U_i}{4\pi\epsilon_0} \sum_{j=-\infty, j\neq i}^{\infty} \frac{c_j U_j (z_i - z_j)}{r_{i,j}^3} \end{aligned} \tag{9}$$

since $(z_i - z_j)^2 / r_{i,j}^2 \approx 0$. Clearly $F_{\text{elec},i}^{\perp}$ tends to a constant, as $r_{i,j}$ goes to infinity. A plot of the electrostatic coupling force, in which we assume extreme deflection of the microcantilevers from their mean position (100 nm), is shown in Figure 2(a). Fifteen neighbors are considered on either side of the reference microcantilever. The force clearly levels off with the increase in the number of neighbors suggesting that the effect of electrostatic coupling is localized, i.e. only a few neighbors appear to contribute.

2.3. Spatial invariance

The system is treated as being spatially invariant in nature since the same dynamical model holds for each microcantilever. The generalized nonlinear equation of motion for the ith microcantilever is now given by

$$\begin{aligned} \ddot{z}_i + b\dot{z}_i + \omega^2 z_i = {} & \frac{\epsilon_o A}{2md^2}\left(1 + \frac{2z_i}{d}\right) U_i^2 \\ & + \frac{1}{m} \sum_{j=i-1, \neq i}^{j=i+1} \gamma_{i,j}(z_j - z_i) \\ & + \frac{c_i U_i}{m 4\pi\epsilon_0} \sum_{j=-\infty, j\neq i}^{\infty} \frac{c_j U_j (z_i - z_j)}{r_{i,j}^3} \end{aligned} \tag{10}$$

We assume the equilibrium values for the states $z_i, \dot{z}_i$, and U_i are respectively given by z_e, 0, and U_e, and we define $x_{i1} := z_i - z_e$, $x_{i2} := \dot{z}_i$, $x_{e1} := z_e$, $V_i := U_i - U_e$, and $V_e := U_e$. Since

$$c_i = \frac{\epsilon_0 A}{(d - z_i)} = \frac{\epsilon_0 A}{d}\left(1 + \frac{z_i}{d} + \left(\frac{z_i}{d}\right)^2 + \ldots\right)$$

as $d > z_i$, using the first-order approximation of c_i we can write the linearized equation of motion for the above model in the state space form as follows:

$$\dot{x}_{i1} = x_{i2} \tag{11}$$

$$\begin{aligned} \dot{x}_{i2} = {} & -bx_{i2} - x_{i1}\left(\omega^2 - \frac{\epsilon_0 A V_e^2}{md^3}\right) \\ & + \left(\frac{2x_{e1}\epsilon_0 A V_e}{md^3} + \frac{\epsilon_0 A V_e}{md^2}\right) V_i \\ & - \left(1 + \frac{x_{e1}^2}{d^2} + \frac{2x_{e1}}{d}\right) \epsilon_0 \frac{A^2 V_e^2}{d_m^2 4\pi} \sum_{j=-\infty, j\neq i}^{\infty} \frac{\delta x_{1ji}}{r_{i,j}^3} \\ & + \frac{1}{m} \sum_{j=i-1, j\neq i}^{j=i+1} \gamma_{i,j} \delta x_{1ji} \end{aligned} \tag{12}$$

where $\delta x_{1ji} = x_{j1} - x_{i1}$. We point out here that the efficacy of the above linearized model is shown later in the paper through simulations of the nonlinear model. The current generated as a result of the excitation of microcantilevers is considered to be the output of the system and its expression is given as $y_i = d(c_i V_i)/dt$. Using again the first-order approximation for c_i, we have

$$y_i = V_i \frac{\epsilon_0 A}{d^2} x_{i2} + \frac{\epsilon_0 A}{d} \dot{V}_i + \frac{\epsilon_0 A x_{i1}}{d^2} \dot{V}_i \tag{13}$$

After linearizing the above equation around the equilibrium and with $\dot{U}_i = 0$, we obtain

$$y_i = \frac{V_e \epsilon_0 A}{d^2} x_{i2} + \dot{V}_i \left(\frac{\epsilon_0 A}{d} + \frac{\epsilon_0 A x_{e1}}{d^2}\right)$$

2.4. Spatio-temporal scaling

We employ spatio-temporal scaling to improve the computational efficiency of the system. In doing so, we define $[\hat{x}_{i1}\ \hat{x}_{i2}]^{\mathrm{T}} = \delta_x [x_{i1}\ x_{i2}]^{\mathrm{T}}$, $\hat{y}_i = \delta_y y_i$, $\hat{V}_i = \delta_V V_i$, and $\tau = \omega_0 t$, where δ_x, δ_y, δ_V and ω_0 are scaling factors. Scaling factors of the order of inverse of the system dimensions in standard units (e.g. SI units) seem to work well. For example, for a natural frequency of

about 50 kHz for the given system, a scaling factor of $\omega_0 = 10^3$ worked well. Likewise, given that the length of the system was about 200 μm, a scaling factor of $\delta_x = 10^6$ was chosen, and for an applicable voltage in the range of millivolts, $\delta_v = 10^3$ worked well. We now define the following:

$$a_{11} = 0, \quad a_{12} = 1, \quad a_{22} = -\frac{b}{\omega_0}$$

$$a_{21} = -\frac{\omega^2}{\omega_0^2} + \frac{\epsilon_0 A \hat{V}_e^2}{\omega_0^2 m d^3 \delta_V^2} - \frac{1}{m\omega_0^2} \sum_{j=i-1, j\neq i}^{i+1} \gamma_{i,j} + \left(1 + \frac{\hat{x}_{e1}^2}{d^2\delta_x^2} + \frac{2\hat{x}_{e1}}{d\delta_x}\right) \epsilon_0 \frac{A^2 \hat{V}_e^2}{d^2 m 4\pi\omega_0^2 \delta_V^2} \sum_{j=-\infty, j\neq i}^{\infty} \frac{1}{r_{i,j}^3}$$

and

$$\hat{A} = \begin{bmatrix} a_{11} & a_{12} \\ a_{21} & a_{22} \end{bmatrix}, \quad \hat{B} = \begin{bmatrix} 0 \\ \frac{\delta_x}{\delta_V}\left(\frac{2\hat{x}_{e1}\epsilon_0 A \hat{V}_e}{m d^3 \omega_0^2 \delta_V^2} + \frac{\epsilon_0 A \hat{V}_e}{m d^2 \omega_0^2}\right) \end{bmatrix}$$

$$\hat{G}_{i,j} = \sum_{j\neq i} \begin{bmatrix} \frac{1}{m\omega_0^2}\gamma_{i,j} - \left(1 + \frac{\hat{x}_{e1}^2}{d^2\delta_x^2} + \frac{2\hat{x}_{e1}}{d\delta_x}\right) \times \epsilon_0 \frac{A^2 \hat{V}_e^2}{d^2 m 4\pi\omega_0^2 \delta_V^2} \frac{1}{r_{i,j}^3} & 0 \\ 0 & 0 \end{bmatrix}$$

where we have used $\gamma_{i,i+k} = 0$ for $|k| > 1$. Extending the state variables to include $\hat{x}_{i3} = \hat{V}_i$, the state space formulation is modified as follows;

$$\tilde{A} = \begin{bmatrix} \hat{A} & \hat{B} \\ 0 & 0 \end{bmatrix}, \quad \tilde{B} = \begin{bmatrix} 0 \\ 0 \\ 1 \end{bmatrix}, \quad \tilde{G}_{i,j} = \begin{bmatrix} \hat{G}_{i,j} & 0 \\ 0 & 0 \end{bmatrix},$$

$$\tilde{C} = \begin{bmatrix} 0 & \frac{\hat{V}_e \epsilon_0 A}{d^2} & 0 \end{bmatrix}, \quad \tilde{D} = \left[\frac{\delta_x}{\delta_V}\omega_0\left(\frac{\epsilon_0 A}{d} + \frac{\epsilon_0 A \hat{x}_{e1}}{d^2}\right)\right].$$

The entire system can now compactly be written for the ith microcantilever as follows:

$$\dot{\hat{x}}_i = \tilde{A}\hat{x}_i + \sum_{j=-\infty, j\neq i}^{\infty} \tilde{G}_{i,j}\hat{x}_j + \tilde{B}\dot{\hat{V}}_i \tag{14}$$

$$\hat{y}_i = \tilde{C}\hat{x}_i + \tilde{D}\dot{\hat{V}}_i \tag{15}$$

3. Controller design

We have seen in the previous section that the system under consideration is of infinite dimension and has a spatially invariant structure. Implementation of a centralized controller for such systems is impractical. A need hence arises for a controller that has a localized structure and whose performance is comparable to that which can be achieved by the ideal scheme of a centralized controller. This motivates us to first look at the performance of a centralized controller given a small (finite) subsystem of the original (infinite-dimensional) system. From a practical viewpoint we, however, consider the following two control schemes with localized architecture: (a) a $\mathcal{H}_\infty$ decentralized controller that completely ignores the dynamics contributed by the neighbors hence treating them as an external disturbance, (b) a $\mathcal{H}_\infty$ distributed controller that makes use of information only from its immediate neighbors. As we show in the sections to follow, a $\mathcal{H}_\infty$ decentralized controller falls short by 100% in terms of performance when compared with a centralized controller. On the other hand, a $\mathcal{H}_\infty$ distributed controller matches well to a centralized controller in terms of performance and hence is an obvious choice for practical design implementation.

In line with the above discussion, we present in this section the three control designs previously mentioned in the following order; (1) centralized, (2) decentralized, and (3) distributed. The performance of these controllers is tested via simulations of the finite-dimensional nonlinear model of the system. We also establish robust performance bounds for the distributed controller and test them via simulations of the linear and the nonlinear model of the system.

3.1. Centralized controller design for a small array

In this section we design a suboptimal $\mathcal{H}_\infty$ centralized controller for a small array of eight microcantilevers. The motivation of this design is to have some sort of benchmark performance index to compare with simpler and practically feasible schemes for large arrays such as the decentralized one and the distributed one to appear later in this paper.

3.1.1. Linear fractional transformation formulation.

Using the model developed in the previous section, the state space model for an eight microcantilever system can be expressed as

$$\dot{\hat{x}} = A\hat{x} + B_1 w + B_2 \dot{\hat{u}}, \ \hat{y} = C\hat{x} + D\dot{\hat{u}} \tag{16}$$

where $\hat{y} \in \mathbb{R}^{8\times 1}$ is the output vector containing the current measured from each microcantilever. The state vector $\hat{x} \in \mathbb{R}^{24\times 1}$ contains the states of eight subsystems, each subsystem contributing three states. Here $w \in \mathbb{R}^{8\times 1}$ represents the disturbance vector entering the system through the input channel; each component of which is assumed to enter each subsystem individually. We use $\dot{\hat{u}} \in \mathbb{R}^{8\times 1}$ to denote the vector of control input (which is the time derivative of the voltage); each component of which is in turn the control input for each subsystem individually. We now define the following for the

linear fractional transformation (LFT) setup shown in Figure 3, where P and K represent the plant and the controller respectively.

Here

$$\tilde{y} = \begin{bmatrix} \hat{y} \\ \hat{u} \\ r \end{bmatrix}; \quad \tilde{z} = \begin{bmatrix} \tilde{r} - \tilde{x}_1 \\ \tilde{u} \\ \bar{u} \end{bmatrix}; \quad \tilde{w} = \begin{bmatrix} w \\ d \\ r \end{bmatrix};$$

and $\hat{u} = \hat{V} \in \mathbb{R}^{8\times 1}$ is the integral of the control input (i.e. consists of applied voltage) for the microcantilever array consisting of eight members. The vector $z_u = \tilde{u} = W_u \hat{V} \in \mathbb{R}^{8\times 1}$ is the weighted rate of change of the input voltage; $z_{\hat{u}} = \bar{u} = W_{\hat{u}} \hat{u} \in \mathbb{R}^{8\times 1}$ is the weighted input voltage; $z_e = \tilde{r} - \tilde{x}_1 = W_e(r - x_1) \in \mathbb{R}^{8\times 1}$ is the weighted tracking error for the eight microcantilevers, where $r \in \mathbb{R}^{8\times 1}$ is the reference command, and $x_1 \in \mathbb{R}^{8\times 1}$ is the vector consisting of the microcantilever tip positions for the eight microcantilever systems. Here $w \in \mathbb{R}^{8\times 1}$ and $d \in \mathbb{R}^{8\times 1}$ are the vectors representing any external disturbance entering the subsystems, and the measurement noise in the output channels, respectively. The design weights W_u and $W_{\hat{u}}$ are chosen so that the control effort does not exceed the allowable limit of ± 7.5 V as per Napoli et al. (2004) and its rate of change remains reasonable. We choose W_e to control the device bandwidth, W_w is chosen to attenuate the effect of any external disturbance entering the system at the input channel, and W_d is chosen such that the effect of high-frequency measurement noise on the system output is attenuated. We define bandwidth as the maximum excitation frequency where the tracking error remains less than or equal to ± 2 nm.

3.1.2. Controller design and simulation of nonlinear system.

MATLAB's Robust Control Toolbox was used to design a centralized controller to meet the specifications stated in the previous section. A controller with an order of 40 was obtained. Simulations of the linear system with the centralized controller suggest that a maximum bandwidth of 10,000 rad s^{-1} can be achieved before utilizing excessive control effort. In the simulation of the nonlinear system, however, a resonance-like phenomenon is experienced when the excited frequency is increased beyond a frequency of 3,000 rad s^{-1}, thus limiting the operable bandwidth (for details see Sarwar (2006)). The designed controller was tested on a model that consisted of an array of eight microcantilevers. The system output (current) from each microcantilever was passed on to the centralized controller. A reference sinusoidal input with a frequency of 3,000 rad s^{-1} and 10 nm amplitude was applied to each microcantilever. Nonlinear behavior of the system was observed upon increasing the amplitude beyond 10 nm. The reference inputs, however, had different (and independent) phase shifts. The absolute tracking error plots for the array system is presented in Figure 4(a). Also, the reference input along with the tracked output for two sample microcantilevers is presented in Figure 4(b). The tracking error is seen to remain bounded within ± 1.75 nm. It is interesting to note that when the excitation frequency is changed across the microcantilever array, the system does not suffer any loss in terms of performance, thus lending added flexibility to the device that may be exploited in certain applications. Plots depicting the performance of the designed centralized controller under varying excitation frequencies across it members (microcantilever) can be found in Sarwar (2006) and has been omitted here for brevity. We comment here that the non-zero tracking error exhibited in the above referred plots is a consequence of operating the device near the limiting bandwidth (3,000 rad s^{-1}) in addition to some linear approximation error of the nonlinearities in the given system when excited at an amplitude of 10 nm. The tracking error is seen to decrease when the excitation amplitude (which acts as a perturbation around the linearized point) is decreased for the same excitation frequency (3,000 rad s^{-1}).

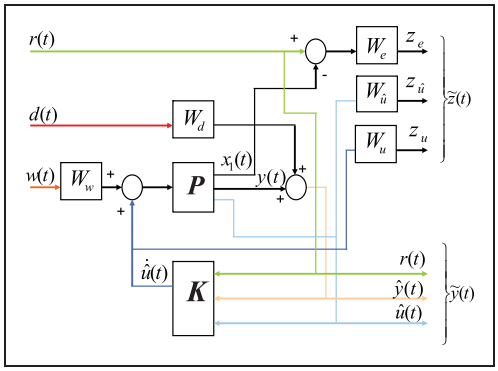

Figure 3. Setup for the linear fractional transformation (LFT) formulation.

3.2. Decentralized controller design

In this section we address the design objectives discussed earlier by designing a decentralized controller. We treat the dynamical coupling as an external disturbance and try to minimize the $\mathcal{H}_\infty$ norm of the transfer function T_{zw}, where w captures the coupling effects, other disturbances, and modeling uncertainties, while z represents the control variables to be kept small (tracking error, control effort, and the rate of control effort). The performance of the designed controller is tested via simulations of the nonlinear system.

3.2.1. Control design and simulation of the nonlinear system.

Following the steps described previously, we

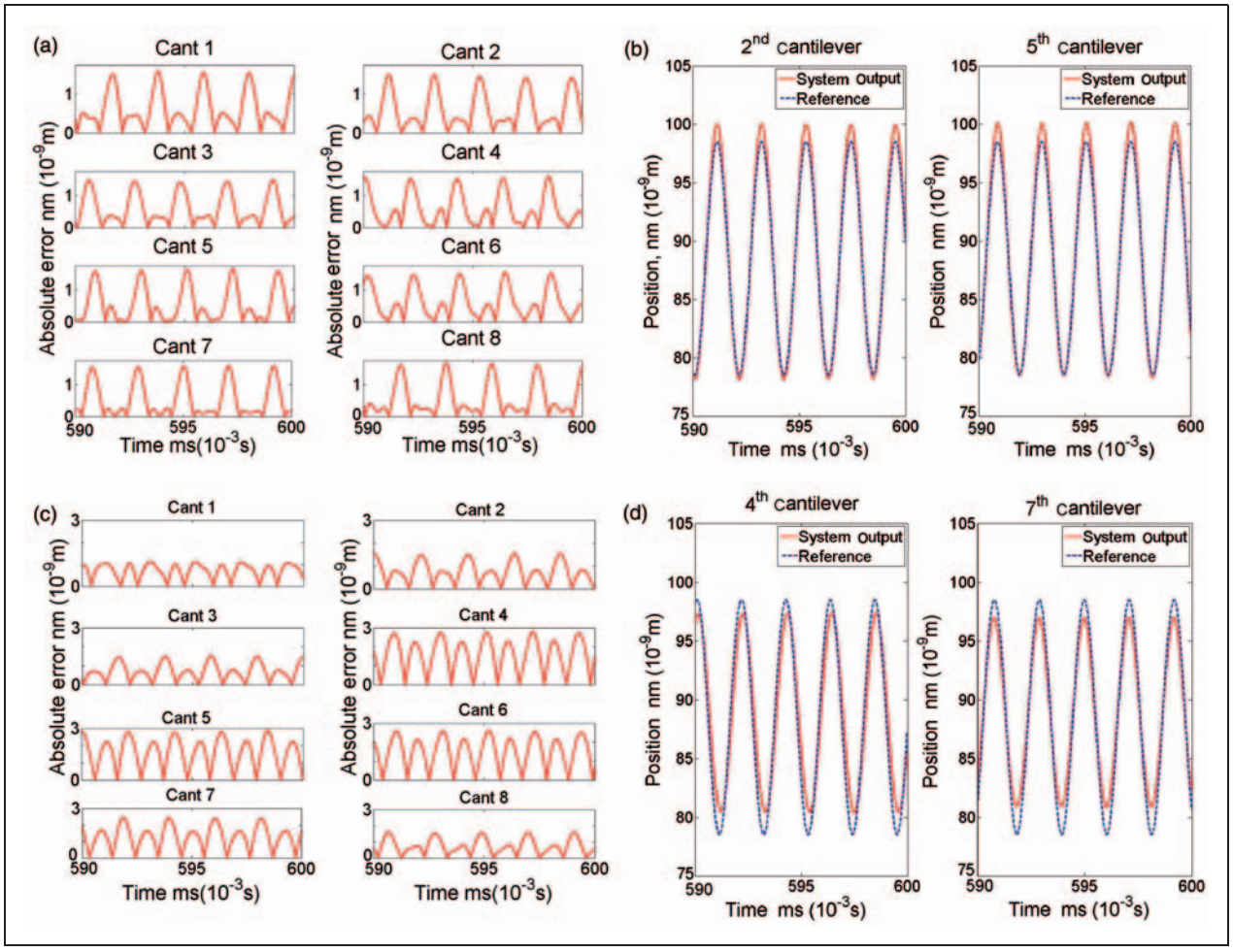

Figure 4. (a), (b) Centralized control design: (a) tracking error for the system of eight cantilevers and (b) reference input and tracked output for two sample cantilevers at the same excitation frequency. (c), (d) Decentralized control design: (c) tracking error and (d) reference input and tracked output for two sample cantilevers at the same excitation frequency. In all of the above cases the excitation (sinusoid) frequency and amplitude are 3,000 rad s^{-1} and 10 nm, respectively.

formulate the LFT for the system in question. The general LFT setup is again represented by Figure 3, where the signal w now also captures the effects of dynamical coupling entering the system along with any other possible disturbances while the plant is totally decoupled. This scheme resulted in a fifth-order controller (at each station) with a bandwidth of 8,500 rad s^{-1} for the linear system. The controller was tested on a nonlinear model that consisted of an array of eight microcantilevers. The dynamical coupling effects were passed amongst the neighbors, but were seen as elements of an external disturbance by the controller. As before, reference sinusoidal inputs with a frequency of 3,000 rad s^{-1} and 10 nm amplitude with independent phase were applied to each microcantilever (see Figure 4(c)). Also, the reference input along with the tracked output for two microcantilevers is presented in Figure 4(d). It can be seen that the system suffers an absolute tracking error of less than 3 nm. This error bound is about 70% more than that for the centralized controller. The performance of this design aggravates further if the frequency of excitation is varied across the microcantilevers and the bound for absolute tracking error further increases to 4 nm.

3.3. Distributed controller design

We have seen in the last section that the resolution achieved by a decentralized controller is not comparable to that achieved by a centralized one and deteriorates by about 70%. It further degrades by about 200% when the excitation frequency is changed across the device, hence making this scheme impractical when a finer resolution is required. The theory of distributed control addresses this issue and helps in achieving a localized controller architecture given a desired performance.

With this motivation, we apply the recent results of distributed control (Bamieh et al., 2002) to our system in this section and compare the resulting performance with that of the benchmark performance delivered by the centralized controller. We also analyze the robust performance (Gorinevsky and Stein, 2003) of the ensuing distributed controller and verify the robust performance margins via simulations of the linear and nonlinear model of the system.

3.3.1. Spatially invariant formulation. Let x_i in Figure 5 denote the state of the corresponding segment, i.e. $x_i = [x_{i1}, x_{i2}, x_{i3}]'$, where x_{i1} is the position of the tip of microcantilever, x_{i2} is the velocity of the microcantilever tip, and x_{i3} is the applied voltage. Define the spatial shift operator S by $x_1 = Sx_0$, $x_{-1} = S^{-1}\ x_0$. The state of the kth microcantilever can be expressed in the form of $S^k\ x_0$, where $k \in \mathbb{Z}$. The dynamics of each segment are

$$\begin{aligned} \dot{x}_i &= A(S)x_i + B_1 w_i + B_2 u_i \\ y_i &= Cx_i + Du_i + d_i \end{aligned} \tag{17}$$

where u_i is the rate of applied voltage, w_i captures any external disturbance effects such as moisture and external vibration effects on each element, and d_i is the noise in the output. Note that in (17), B_1, B_2, C, D, and d do not have any spatial spread and, therefore, are not functions of S. The system dynamics in Equation (17) are entirely captured in $A(S)$, which is given by

$$\begin{aligned} A(S) = \cdots A_{-3}S^{-3} + A_{-2}S^{-2} + A_{-1}S^{-1} + A_0 \\ + A_1 S + A_2 S^2 + A_3 S^3 \cdots = \sum_{j=-\infty}^{\infty} A_j S^j \end{aligned} \tag{18}$$

where for a given i, $A_0 = \tilde{A} - \sum_{j=-\infty, j\neq i}^{\infty} \tilde{G}_{i,j}$, and $A_j = \tilde{G}_{i,j}$ (see Equation (14)). As it is evident from Equation (18), the state equation takes into account the dynamic coupling effects from infinitely many of its neighbors. Of those, however, only finitely many are significant as shown earlier. What we seek here is, hence, a controller for each element that could use information from only a finite number of its neighbors and meet the performance objectives without any significant loss.

The spatial shift operator (S^j) corresponds to multiplication by $e^{j\theta}$ in the frequency domain, hence, when applying the $\mathcal{H}_\infty$ distributed control methods of Bamieh et al. (2002), we need to evaluate the spatial shift operator $S = e^{j\theta}$ over the interval $[0, 2\pi]$. Approximations of the state space matrices $A_c(S)$, $B_c(S)$, $C_c(S)$, and $D_c(S)$ for the distributed controller can be obtained by considering only a finite number of expressions in terms of the spatial operator S.

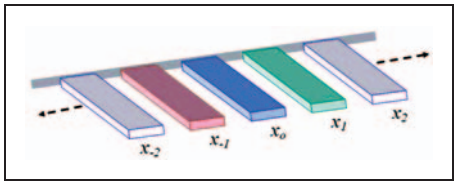

Figure 5. Spatially invariant framework.

Since the microcantilevers are spatially invariant, and symmetric, we approximate, for example, the state matrix $A_c(S)$ by the symmetric group of operators in S and S^{-1}. An approximation using only three neighbors on either side, which has seven terms, is as follows:

$$\begin{aligned} A_c(S) = A_{c_{-3}}S^{-3} + A_{c_{-2}}S^{-2} + A_{c_{-1}}S^{-1} + A_{c_0} \\ + A_{c_1}S + A_{c_2}S^2 + A_{c_3}S^3 \end{aligned} \tag{19}$$

The coefficient matrices A_{c_i} of the expansion can be determined using least-squares estimation (LSE)-based methods (Ljung, 1987). To illustrate the procedure, we calculate the seven coefficient matrices in Equation (19). Let n denote the dimension of the matrix $A_c(S)$, and with slight abuse of notation, we use $A_c(k)$ to represent the value of the operator $A_c(S)$. Let m be the number of gridding points of Fourier frequencies θ, then $A_c(k)$ at the kth gridding point of the Fourier frequency θ is given by $A_c(k) =$

$$\begin{aligned} &(I_n e^{-3j\theta_k}, I_n e^{-2j\theta_k}, I_n e^{-j\theta_k}, I_n, I_n e^{j\theta_k}, I_n e^{2j\theta_k}, I_n e^{3j\theta_k}) \\ &\quad \times (A_{c_{-3}}, A_{c_{-2}}, A_{c_{-1}}, A_{c_0}, A_{c_1}, A_{c_2}, A_{c_3})^* \\ &:= \psi_k \times \Omega \end{aligned} \tag{20}$$

where Ω is the real coefficient matrix of $(A_{c_{-3}}, \ldots, A_{c_0} \cdots A_{c_3})^*$, and $j = \sqrt{-1}$.

Since at each Fourier frequency point θ, the value of ψ_k is easily calculated and the matrix $A_c(S)$ is the state matrix of the controller, stacking all of the Equations (20) at every gridding point, we obtain

$$\begin{pmatrix} A_c(1) \\ A_c(2) \\ \vdots \\ A_c(m) \end{pmatrix} = \begin{pmatrix} \psi_1 \\ \psi_2 \\ \vdots \\ \psi_m \end{pmatrix} \Omega \tag{21}$$

or

$$A_c = \Phi \times \Omega. \tag{22}$$

Using the LSE theorem in Ljung (1987), one of the best coefficient matrix estimates is given by

$$\begin{aligned} \Omega = &[(\mathrm{Re}\,\Phi)'(\mathrm{Re}\,\Phi) \\ &+ (\mathrm{Im}\,\Phi)'(\mathrm{Im}\,\Phi)]^{-1} \begin{pmatrix} \mathrm{Re}\,\Phi \\ \mathrm{Im}\,\Phi \end{pmatrix}' \begin{pmatrix} \mathrm{Re}\,A_c \\ \mathrm{Im}\,A_c \end{pmatrix} \end{aligned} \tag{23}$$

where Re denotes the real part and Im denotes the imaginary part.

For better approximation of $A_c(S)$, higher-order polynomials of S, S^{-1} can be used. The $\mathcal{H}_\infty$ controller is described as

$$\begin{aligned} \dot{x}_c &= A_c x_c + B_c y_c \\ u_c &= C_c x_c + D_c y_c \end{aligned} \tag{24}$$

In the case of approximation (19), the structure of the controller is given as

$$\begin{aligned} \dot{x}_c &= [A_{c_{-3}} S^{-3} + \cdots + A_{c_0} + \cdots + A_{c_3} S^3] x_c \\ &\quad + [B_{c_{-3}} S^{-3} + \cdots + B_{c_0} + \cdots + B_{c_3} S^3] y_c \\ u_c &= [C_{c_{-3}} S^{-3} + \cdots + C_{c_0} + \cdots + C_{c_3} S^3] x_c \\ &\quad + [D_{c_{-3}} S^{-3} + \cdots + D_{c_0} + \cdots + D_{c_3} S^3] y_c \end{aligned} \tag{25}$$

which means that to calculate the local control, each controller needs to communicate with six cantilevers and controllers in its immediate neighborhood (three on either side).

3.3.2. Controller spatial truncation. Figure 6(a) shows a Bode magnitude plot, at different gridding points of the Fourier frequency θ, for reference to error transfer function for a single microcantilever when the controller uses information from its 10,000 neighbors (5,000 on each side). The localization of the coupling effects on the ith microcantilever permits the formulation of a control law that entertains only the information from its immediate neighbors and yet delivers performance that is comparable to the full information controller. The Bode magnitude plot of the reference to error transfer function at various Fourier frequencies θ for this case is shown in Figure 6(b). Note that the system does not suffer any loss of bandwidth as compared with the case in Figure 6(a) discussed above. In both of the cases discussed above, the order of the distributed controller was five.

3.3.3. Simulation of the nonlinear model. In the following we present results of the simulation carried out to verify the performance of the truncated controller as suggested by Figure 6(b). We simulate the truncated controller on a 10-segment nonlinear system of microcantilever array. This results in each microcantilever having an asymmetric neighborhood of nine microcantilevers. Each controller was in communication with only two of its neighbors (one on each side) and was also receiving information for the system output (current measured) from two of its neighboring microcantilevers except for the controllers at the edge of the array. The controllers at the edge were truncated such that no information was passed to them from their neighbors. Asymmetric truncation of the controllers at the edge was seen to cause destabilization. The reference input was fixed at a frequency of 3,000 rad s^{-1}, with an amplitude of about 10 nm. The reference inputs, however, had different

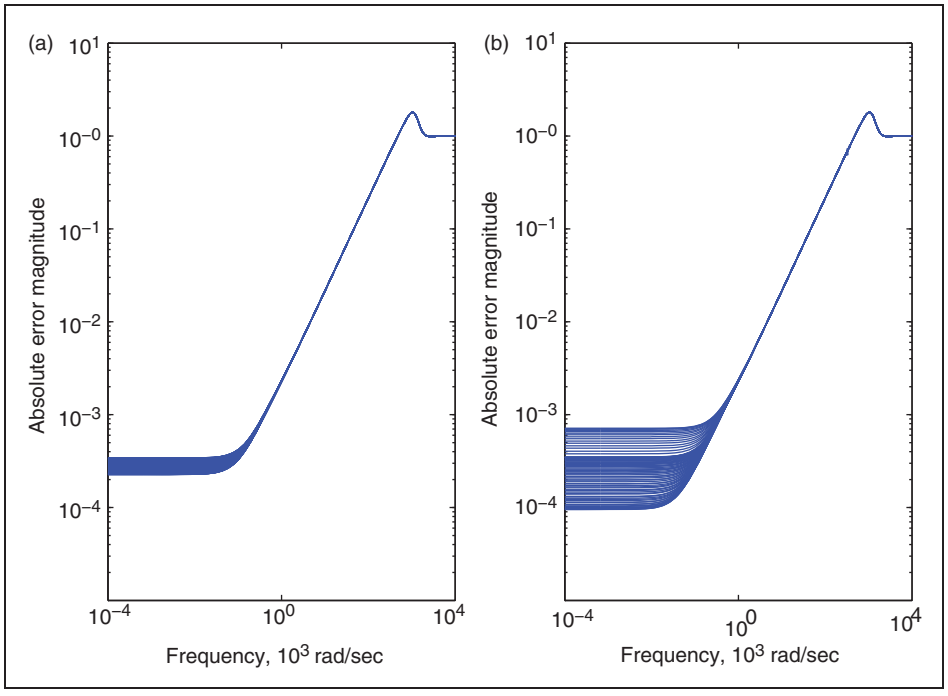

Figure 6. Bode magnitude plot for reference to the error transfer function for the ith microcantilever using controllers utilizing: (a) information from 10,000 neighbors (5,000 on each side); and (b) information from only two neighbors (one on each side).

(and independent) phase shifts. The resulting absolute tracking error plots are presented in Figure 7(a).

It is seen from these plots that the controller truncation at the edge results in performance degradation at the edge microcantilevers and their immediate neighbors. The lack of information at the edge microcantilevers results in the propagation of tracking error to their immediate neighbors. This tracking error propagation is, however, localized and the nonimmediate neighbors do not get affected. This is evident from the fact that an absolute error bound of 1.75 nm is observed at the nonimmediate neighbors of the edge microcantilevers as opposed to 5 nm, and 25 nm which is observed for the immediate neighbors of the edge microcantilevers and the edge microcantilevers, respectively. This resolution is comparable to what is achieved when a centralized controller is employed for a system of eight microcantilever array as discussed in Section 3 above. The sample plots for the nonimmediate neighbors of the edge microcantilevers are presented in Figure 7(b). When the frequency of excitation was changed across the microcantilevers, the same level of tracking error bound was experienced for the edge microcantilevers, their immediate neighbors, and their nonimmediate neighbors as discussed above (see Figure 8(a)). Also, a sample plot for the case when excitation frequency is changed across the device is presented in Figure 8(b).

The system was also simulated to track a triangular wave. The reference input was fixed at a frequency of 700 rad s^{-1}, with an amplitude of about 10 nm. The reference inputs, however, had different (and independent) phase shifts. The resulting absolute tracking error plots are presented in Figure 8(c), and a sample plot is presented in Figure 8(d). It can be seen from these plots that absolute tracking error at the nonimmediate neighbors of the edge microcantilevers remain bounded within 1.75 nm.

3.3.4. Robustness analysis. We have seen above that the distributed controller performs quite satisfactorily for the nominal plant. In practice, the actual system may differ from the nominal plant. In particular, in our case the dynamics of each microcantilever can be slightly different from the rest owing largely to the lack of perfect control in the process of fabrication. It is, therefore, of interest to establish some sort of allowable bounds on the variation on the nominal system given the design of the distributed controller of the previous section. In other words, we pose the following question: to what degree can the parameters of the nominal system be varied before the performance delivered by the distributed controller starts to degrade? In order to answer this question, we carry out a robust performance analysis of the designed controller using the theoretic tools found in Gorinevsky and Stein (2003). The system considered is described by the standard block diagram of Figure 9(a): where $w = \tilde{w}$ and $z = \tilde{z}$ carry the same definitions as above in the LFT formulation. Let $\hat{M}(s, \lambda)$ be a stable closed-loop transfer function which is formed by the lower fractional transformation $\hat{G}(s, \lambda)$ of the linearized system with the designed controller $\hat{K}(s, \lambda)$, that is,

$$\hat{M}(s, \lambda) := F_l(\hat{G}(s, \lambda), \hat{K}(s, \lambda)),$$

where s and λ represent Laplace and Fourier transform variables, respectively. The perturbation Δ to the

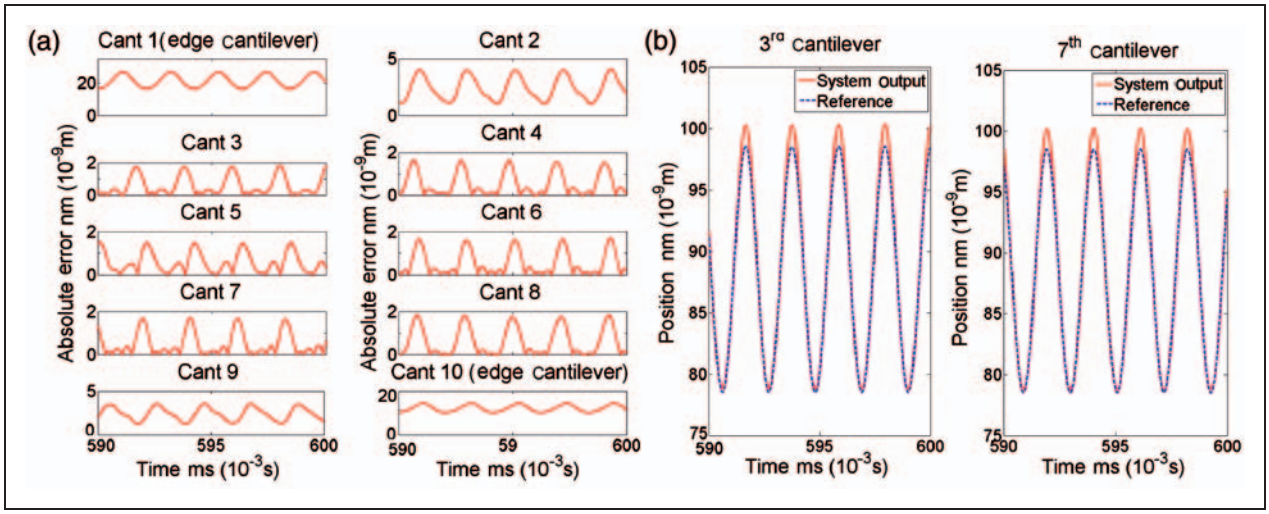

Figure 7. (a) Tracking error for the array system of 10 cantilevers and (b) reference input and tracked output at same excitation frequency (3,000 rad s^{-1} sinusoid, 10 nm amplitude) using truncated distributed controller.

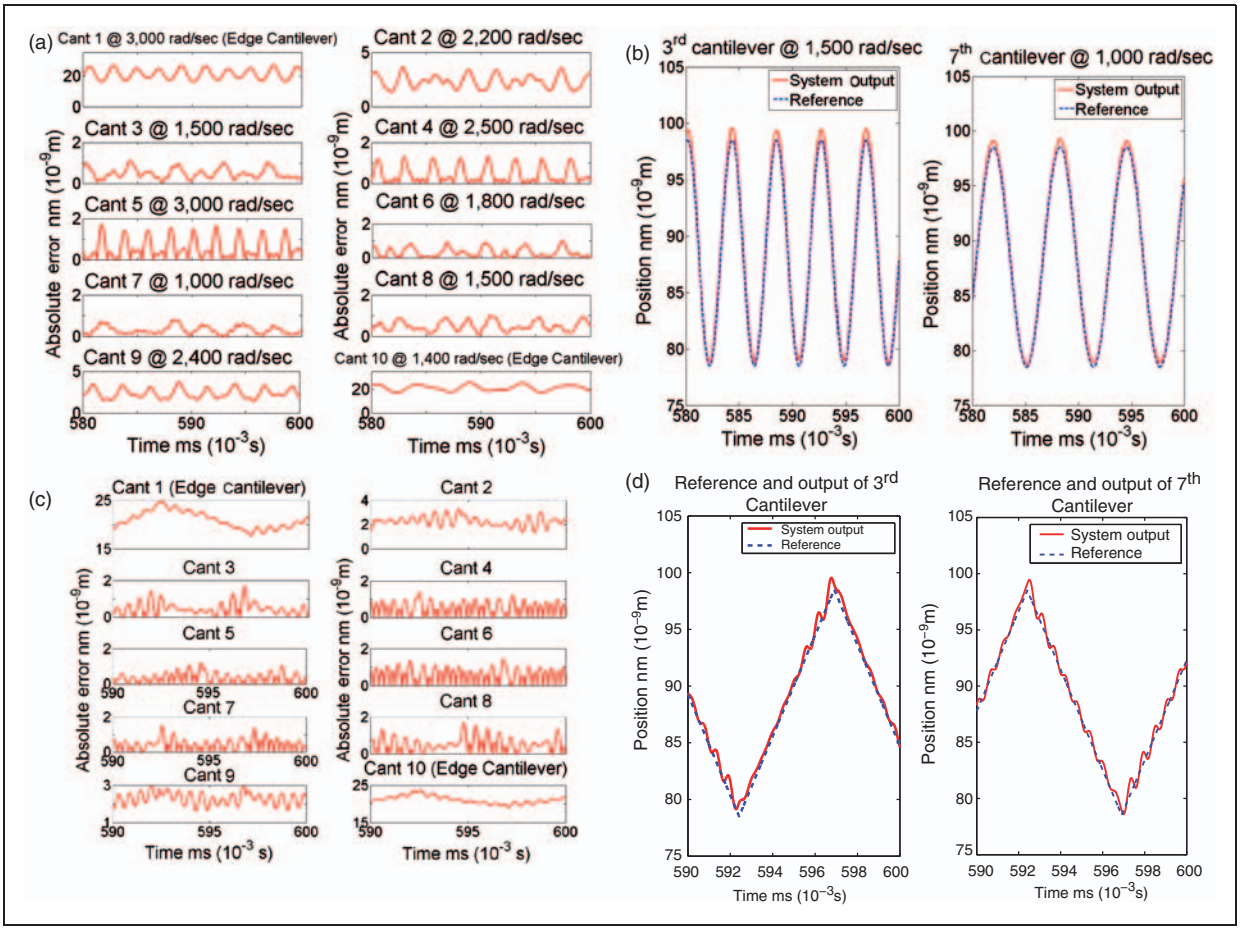

Figure 8. (a) Tracking error for the array system of 10 cantilevers at different excitation frequencies (sinusoids, 10 nm amplitude) using truncated distributed controller. (b) Reference input and tracked output at different excitation frequencies (sinusoids, 10 nm amplitude) using truncated distributed controller. (c) Tracking error for the array system of 10 cantilevers at the same excitation frequencies. (d) Reference input and tracked output at the same excitation frequencies (700 rad s^{-1} triangular waves, 10 nm amplitude) using a truncated distributed controller.

nominal model is defined as having the following usual block diagonal structure:

$$\Delta = \{\mathrm{diag}[\delta_1 I_{r1}, \ldots, \delta_s I_{rs}, \Delta_1, \ldots, \Delta_F] : \delta_i \in \mathbb{C}, \quad \Delta_j \in \mathbb{C}^{m_j \times m_j}\}, \tag{26}$$

where the block structure and block dimensions depend on the specific type of perturbations considered in the model.

For robust performance analysis we also define the standard (Gorinevsky and Stein, 2003) augmented block,

$$\Delta_p = \begin{bmatrix} \Delta & 0 \\ 0 & \Delta_f \end{bmatrix} \mathbb{C}^{q_2 \times p_2},$$

where Δ has the structure given by (26) and Δ_f is a fictitious block connecting z with w.

3.3.5. Uncertainty modeling and analysis. We consider only the effects of parametric uncertainty in the system of the microcantilever array in order to obtain a 'first-cut' idea of the sensitivity of the baseline design. We, therefore, develop herein an uncertainty model to be analyzed. The lumped system parameters (as presented in Section 2) were assumed to have some degree of uncertainty as expressed below. Define:

$$a_{21}(\theta) := \frac{\omega^2}{\omega_0^2} + \frac{\epsilon_0 A \hat{V}_e^2}{\omega_0^2 m d^3 \delta_V^2} + \frac{1}{m\omega_0^2} \sum_{m=l-1, m\neq l}^{l+1} \gamma_{l,m}\left(e^{jm\theta} - 1\right) - \left(1 + \frac{\hat{x}_{e1}^2}{\mathrm{d}^2 \delta_x^2} + \frac{2\hat{x}_{e1}}{\mathrm{d}\delta_x}\right) \epsilon_0 \frac{A^2 \hat{V}_e^2}{\mathrm{d}^2 m 4\pi\omega_0^2 \delta_V^2} \sum_{m=-\infty, m\neq l}^{\infty} \frac{1}{r_{l,m}^3}\left(e^{jm\theta} - 1\right)$$

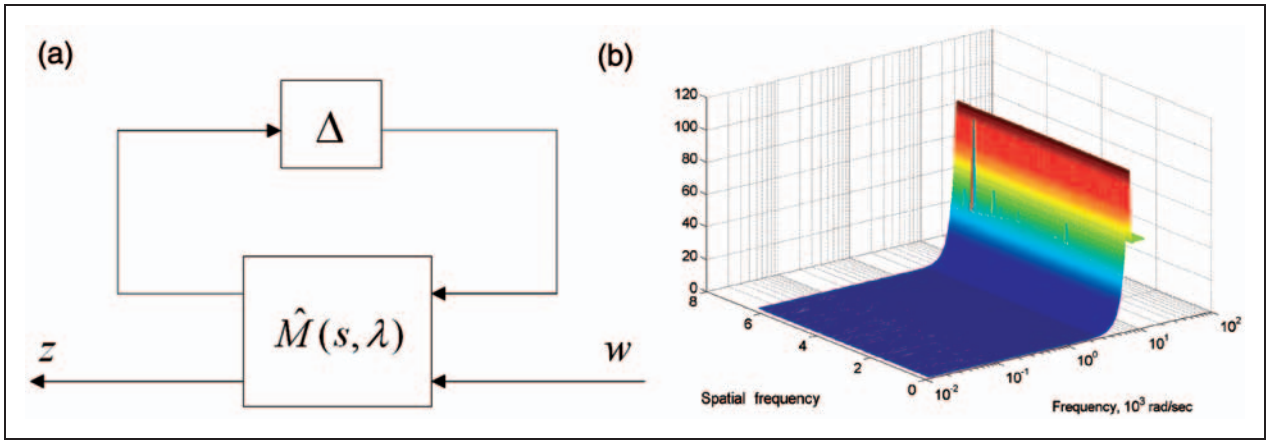

Figure 9. (a) General setup for robust performance; (b) structure singular value plot for robust performance.

$$a_{22} := \frac{b}{\omega_0}, \quad a_{23} := \frac{\delta_x}{\delta_V}\left(\frac{2\hat{x}_{e1}\epsilon_0 A\hat{V}_e}{md^3\omega_0^2\delta_V^2} + \frac{\epsilon_0 A\hat{V}_e}{md^2\omega_0^2}\right),$$
$$c_{62} := \frac{\hat{V}_e\epsilon_0 A}{d^2},$$
$$d_{64} := \frac{\delta_x}{\delta_V}\omega_0\left(\frac{\epsilon_0 A}{d} + \frac{\epsilon_0 A\hat{x}_{e1}}{d^2}\right)$$

and

$$\overline{a_{21}(\theta)} := a_{21}(\theta)(1+\alpha_2\delta_2), \quad \overline{a_{22}} := a_{22}(1+\alpha_1\delta_1)$$
$$\overline{a_{23}} := a_{23}(1+\alpha_3\delta_3), \quad \overline{c_{62}} := c_{62}(1+\alpha_4\delta_4)$$
$$\overline{d_{64}} := d_{64}(1+\alpha_5\delta_5)$$

where $\overline{(\cdot)}$ is the perturbed lumped parameter, and $(\cdot)$ is the nominal value of the lumped parameter. Here $\alpha_i \in \mathbb{R}$ is the percentage uncertainty of the given parameter and $\delta_i \in \mathbb{C}$ is the size of uncertainty the system can tolerate with a reasonable bound on the allowable tracking error. Note that $\overline{a_{21}(\theta)}$ has a spatial structure capturing the uncertainty in the dynamic coupling effects and is a function of Fourier frequency θ. We focus mainly on the transfer function from $w \to e$ (where e is the tracking error) in developing the framework for the uncertainty analysis. A fictitious block $(\Delta_f(\theta))$ of size 3×1 is used in our estimation in order to meet the performance requirement on the tracking error, i.e. keeping the error small. The system was found to be most sensitive to changes in the lumped parameter $a_{21}(\theta)$ that consists of the 'effective natural frequency' squared in addition to the dynamic coupling coefficients. The μ plot of the system as shown in Figure 9(b) permits a 0.44% uncertainty margin for $a_{21}(\theta)$ and a_{23}, while rest of the lumped parameters admit an allowance of 40%.

3.3.6. Perturbation and simulation of the linear system. Random perturbations of varying size were introduced into the nominal system and the operation of an array of 10 such randomly perturbed linear models of microcantilevers was simulated. The allowable uncertainty bounds on $a_{21}(\theta)$ and a_{23}, as established above, were found to be quite conservative as the system was found to tolerate an uncertainty margin of up to 11% on these parameters. This is in line with the fact that the μ analysis is a worst-case analysis and these margins leave a high degree of conservatism. The reference input was fixed at a frequency of 3,000 rad s^{-1} with a magnitude of about 10 nm. The absolute tracking error plot for the perturbed linear system is shown in Figure 10. The error plot is seen to be within a bound of 1.75 nm, a bound that was experienced in the simulation of the nonlinear system.

3.3.7. Perturbation and simulation of the nonlinear system. In order to test the sensitivity of the designed controller to parametric uncertainties for the nonlinear system, random perturbations of varying size in the parameters of natural frequency and the damping coefficient were introduced into the nominal nonlinear models of the microcantilevers. An array consisting of 10 such randomly perturbed nonlinear models of the microcantilever system was simulated. It was found that the designed controller could admit 10% perturbation in the parameter of natural frequency, whereas the damping coefficient could admit 40% perturbation given that the frequency of excitation does not exceed 2,500 rad s^{-1}. Figure 11 presents the absolute tracking error plot for the array consisting of 10 perturbed nonlinear microcantilever systems with a perturbation bound of 10% and 40% on the parameter of natural frequency and damping coefficient, respectively. Again, the absolute error bound can clearly be seen to be with 1.75 nm (an error bound that was achieved for the

nominal nonlinear system) for the nonimmediate neighbors of the edge microcantilevers.

4. Conclusion

In this paper, we have presented a comparison between the centralized, decentralized and the distributed control architectures with respect to tracking performance. Many other performance criteria can be chosen for the comparison. The tracking control of probes is relevant to those applications where probes are oscillated sinusoidally (or any other way) and the effect of the samples being probed are gleaned from the deviations of their actual responses (that reacts to the sample interaction) from the modeled response (that does not account for the sample interaction). The *control* of microcantilevers can seem misleading since they form the sensors (probes) for the sample interaction. One of the ways proposed by Dong and Ferreira (2008) is to use two frequencies as input to the cantilevers, one within and the other outside the control bandwidth, whereby the electrostatic drive can be used simultaneously for *actuating and sensing* the resulting displacement. For instance, to determine the mechanical properties of a sample, one can use amplitude regulation of the the low-frequency signal to negate the effects of, and thereby estimate, the topography, and once the topographic effects are annulled, the high-frequency signal can be used for estimating the sample properties (as used in force modulation microscopy).

In this paper, we presented a model of an infinite array of electrostatically actuated microcantilevers where the effect of mechanical and electrostatic coupling was explicitly taken into account. The electrostatic coupling was weak in nature and only three or four neighbors on either side of a given microcantilever make any significant contribution to it. There exists a notion of spatial invariance for the modeled system in

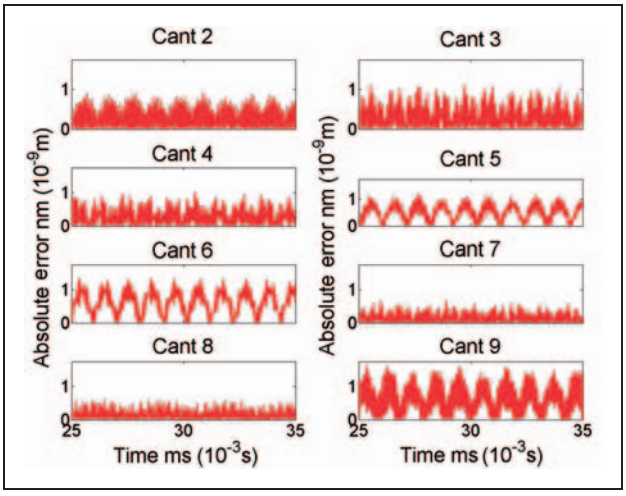

Figure 10. Absolute tracking error plot for the perturbed linear system simulated at 3,000 rad s^{-1} sinusoid, 10 nm amplitude (only nonedge cantilevers are shown).

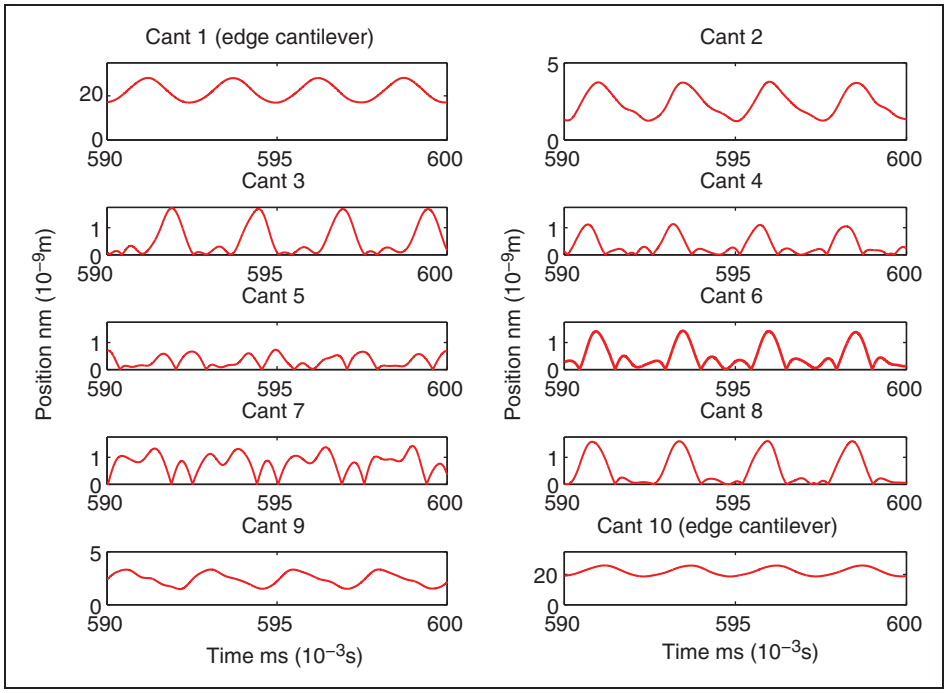

Figure 11. Absolute tracking error plot for the perturbed nonlinear system simulated at 2,500 rad s^{-1} sinusoid, 10 nm amplitude.

the sense that the dynamics of the system are invariant along a spatial axis. The desired performance characterized by a bandwidth of 3,000 rad s^{-1} and a resolution of 1.75 nm can be met by employing a centralized controller on a finite system. The implementation of this approach, however, becomes increasingly complicated as the order of the given system increases. A centralized controller with an order of 40 is required for a system of eight microcantilevers in order to fulfill the task. We have demonstrated that a decentralized control law yields a resolution of 3 nm (70% degradation in comparison to the centralized controller) given that the same excitation frequency is used across the system. This resolution further deteriorates if the excitation frequency is changed across the microcantilevers. This scheme lends a fifth-order decentralized controller (at each station) which is quite amenable in terms of implementation.

The realm of distributed control theory takes care of such systems quite well, which allows the development and implementation of the control law in a distributed fashion, taking into account only the sufficient information necessary for a given performance. This can be seen from the fact that only a fifth-order distributed controller was required irrespective of the number of cantilevers. In particular, we have shown that information from only the immediate neighbors is sufficient to develop a distributed control law that delivers a performance which is comparable to the performance delivered by the centralized controller. For a system of a finite number of microcantilevers, it was observed that the performance of the two edge microcantilevers and their immediate neighbors deteriorates, while the rest of the system meets the performance specification. From an operational point of view, the use of the edge microcantilevers and their immediate neighbors can be abandoned while making use of the rest. We have also demonstrated that the designed controller brings a certain degree of robustness with it. It is important to note here that while we have demonstrated the effectiveness of distributed control architecture and studied its robustness for a specific configuration of a tightly packed microcantilever array system, this scheme can be used in general to address the dynamic couplings of similar systems regardless of the underlying operating principles. Also a wide variety of control schemes, at each unit, can be used for specific performance objectives, communication structures and underlying models (Bamieh and Voulgaris, 2005; Qi et al., 2004).

Acknowledgments

This research is supported in part by NSF Awards CMMI 0800863, CMS 0301516, CNS 0834409 and AFOSR Grant FA 9950-06-1-0252.

References

Bamieh B, Paganini F and Dahleh M (2002) Distributed control of spatially invariant systems. *IEEE Transactions on Automatic Control* 47: 1091–1107.

Bamieh B and Voulgaris P (2005) A convex characterization of distributed control problems in spatially invariant systems with communication constraints. *Systems and Control Letters* 54: 575–583.

Bhushan B (1995) *Handbook of Micro/Nano Tribology*. Boca Raton, FL: CRC Press.

Britton CL, Jones RL, Oden PI, Hu Z, Warmack RJ, Smith SF, et al. (2000) Multiple-input microcantilever sensors. *Ultra-microscopy* 82: 17–21.

Crandall BC (1996) *Nanotechnology: Molecular Speculation on Global Abundance*. Cambridge, Massachusetts: MIT Press.

Despont M, Brugger J, Drechsler U, Dürig U, Höberle W, Lutwyche M, et al. (2000) VLSI-NEMS chip for parallel AFM data storage. *Sensors and Actuators* 80: 100–107.

Dong J and Ferreira P (2008) Simultaneous actuation and displacement sensing for electrostatic drives. *Journal of Micromechanics and Microengineering* 18: 035011.

Gorinevsky D and Stein G (2003) Structured uncertainty analysis of robust stability for multidimensional array system. *IEEE Transactions on Automatic Control* 48: 1557–1568.

Indermühle P-F, Schürmann G, Racine G-A and de Rooij NF (1997) Fabrication and characterization of cantilevers with integrated sharp tips and piezoelectric elements for actuation and detection for parallel AFM applications. *Sensors and Actuators A*60: 186–190.

Ljung L (1987) *System Identification: Theory for the User*. Englewood Cliffs, New Jersey: Prentice Hall, Inc.

Napoli M (2004) *Modeling and Control of Electrostatically Actuated Microcantilever Array*. PhD Thesis, University of California, Santa Barbara.

Napoli M and Bamieh B (2001) Modeling and observer design for an array of electrostatically actuated microcantilevers, in *Proceedings of the 40th IEEE CDC*, Orlando, Florida, pp. 4274–4279.

Napoli M and Bamieh B (2004) Design of a decoupling controller for electrostatically coupled microcantilevers based on current, in *Proceedings of the 2004 American Control Conference*, Boston, Massachusetts, pp. 3134–3139.

Napoli M, Bamieh B and Dahleh M (1998) Optimal control of arrays of microcantilevers, in *Proceedings of the 37th IEEE CDC*, Tampa, Florida, pp. 2077–2082.

Napoli M, Bamieh B and Turner K (2004) A capacitive microcantilever: Modeling, validation and estimation using current measurements. *ASME Journal of Dynamic Systems Measurement and Control* 126: 319–326.

Napoli M, Olroyd C, Bamieh B and Turner K (2005a) A novel sensing scheme for the displacement of electrostatically actuated microcantilevers, in *Proceedings of the 2005 American Control Conference*, Portland, Oregon, pp. 2475–2480.

Napoli M, Zhang W, Turner K and Bamieh B (2003) Dynamics of mechanically and electrostatically coupled microcantilevers, in *12th International*

Conference on TRANSDUCERS, Solid-State Sensors, Actuators and Microsystems, Boston, Massachusetts, pp. 1088–1091.

Napoli M, Zhang W, Turner K and Bamieh B (2005b) Characterization of electrostatically coupled microcantilevers. *Journal of Microelectromechanical Systems* 14: 295–304.

Pantazi A, Sebastian A, Antonakopoulos TA, Bächtold P, Bonaccio AR, Bonan J, et al. (2008) Probe-based ultra-high-density storage technology. *IBM Journal of Research and Development* 52: 493–511.

Sarwar A (2006) *Modeling and Control of Electrostatically Actuated Microcantilever Array*. MS Thesis, University of Illinois Urbana Champaign, Urbana, Illinois.

Qi K, Salapaka PG, Voulgaris PV and Khammash M (2004) Structured optimal control with multiple objectives: A convex solution. *IEEE Transactions on Automatic Control* 49: 1623–1640.

Yves M (1995) *Scanning Probe Microscopes*. Bellingham, Washington: SPIE Press.

Appendix: mechanical characteristics of the system

1. Natural frequency, $\omega = 5.02 \times 10^4$ Hz.
2. Damping coefficient, $b = 20.52$ N·s/m·kg.
3. Coefficient of mechanical coupling, $\gamma_{i,i+1} = \gamma_{i,i-1} = 0.506$ N m^{-1}.
4. Mass of cantilever, $m = 4.6 \times 10^{-11}$ kg.

Remark. Details on sensitivity, control transfer functions, and other transfer functions can be found in Sarwar (2006). They have not been presented here for brevity.